Contradictory nature of Co doping in ferroelectric BaTiO_{3}

Patrick Ponath, Andrew O'Hara, Hai-Xia Cao, Agham B. Posadas, Rama Vasudevan, M. Baris Okatan, S. Jesse, Morgann Berg, Zongyao Li, Desai Zhang, Andrew J. Kellock, Alex de Lozanne, Jianshi Zhou, Sergei Kalinin, David J. Smith, and Alexander A. Demkov

Phys. Rev. B **94**, 205121 — Published 11 November 2016

DOI: 10.1103/PhysRevB.94.205121

The contradictory nature of Co doping in ferroelectric $BaTiO_3$

Patrick Ponath[a], Andrew O'Hara[a], Hai-Xia Cao[b] Agham B. Posadas[a], Rama Vasudevan[c], M. Baris Okatan[c], S. Jesse[c], Morgann Berg[a], Zongyao Li[d], Desai Zhang[e], Andrew J. Kellock[f], Alex de Lozanne[a], Jianshi Zhou[d], Sergei Kalinin[c], David J. Smith[e], Alexander A. Demkov[1a]

[a]Department of Physics, The University of Texas at Austin, Austin, TX 78712, USA
[b]Department of Physics and Jiangsu Key Laboratory of Thin Films
Soochow University, Suzhou, 215006, China
[c]Center for Nanophase Materials Sciences, Oak Ridge National Laboratory, Oak Ridge, TN, 37831, USA
[d]Materials Science and Engineering Program/Mechanical Engineering, University of Texas at Austin, Austin, Texas 78712, USA
[e]Department of Physics, Arizona State University, Tempe, AZ 85287, USA
[f]IBM Almaden Research Center, San Jose, CA, 95120, USA

Abstract

The growth of Co-substituted $BaTiO_3$ (BTO) films on Ge(001) substrates by molecular beam epitaxy is demonstrated. Energy-dispersive X-ray spectroscopy and transmission electron microscopy images confirm the uniform Co distribution. However, no evidence of magnetic ordering is observed in samples grown for Co concentrations between 2-40%. Piezoresponse force microscopy measurements show that a 5% Co-substituted BTO sample exhibits ferroelectric behavior. First-principles calculations indicate that while Co atoms couple ferromagnetically in the absence of oxygen vacancies, the occurrence of oxygen vacancies leads to locally antiferromagnetically coupled complexes with relatively strong spin coupling. The presence of a significant amount of oxygen vacancies is suggested by x-ray photoelectron spectroscopy measurements.

I. Introduction

Multiferroics are materials which simultaneously exhibit at least two of the four primary ferroic orders. However, the current focus of materials research for device development is mainly in the coexistence of ferroelectricity and ferromagnetism [1]. If both of these ferroic orders couple strongly then the electric polarization can be controlled by applying an external magnetic field or *vice versa*. This coupling could pave the way for new technologies and devices, since multiferroic materials could potentially lead to novel spin-based [2-4] or non-volatile data-storage devices [5,6], where information is written electrically and read magnetically. Magnetism and ferroelectricity rarely coexist in single-phase compounds [7,8], and most multiferroics possess low magnetic ordering temperatures [5] even if the ferroelectric transition temperatures

[1] E-mail: demkov@physics.utexas.edu

are above room temperature [9-11]. If ferroelectricity and ferromagnetism are both present in one material, their coupling, which is necessary for device applications, is not guaranteed [12,13]. Most ferroelectric materials are transition metal oxides in which the transition metal atoms possess an empty *d* shell, whereas partially filled *d* shells with unpaired spins are required for ferromagnetism [7].

Two well-known multiferroic materials, crystallizing in a distorted perovskite crystal structure (ABO_3), are $BiMnO_3$ and $BiFeO_3$ [13-16]. In both materials, ferroelectricity is caused by the active 6*s* lone-pair of Bi, while in other ferroelectrics such as $BaTiO_3$ (BTO) the shift of the B atom with respect to the oxygen sublattice causes electric polarization. Due to the fact that ferromagnetism in both $BiMnO_3$ and $BiFeO_3$ is caused by the B-site atom, while ferroelectricity is realized by the displacement of the Bi ion, coupling between the two ferroic orders is weak [13]. Another promising multiferroic material is magnetically-doped compositions of the well-studied ferroelectric $BaTiO_3$. *Ab initio* calculations predict that Cr-, Mn- and Fe-doped BTO are the most promising candidates for ferromagnetism in the transition metal-doped $BaTi_{1-x}TM_xO_3$ system (TM = Sc, V, Cr, Mn, Fe, Co, Ni, Cu) [17-19]. In the work of Nakayama *et al.* [17], only cubic BTO was considered with no additional correlation effects on top of the local spin density approximation, and the formation of oxygen vacancies and their influence on the formation of ferromagnetism was not considered. Several groups have tried to synthesize multiferroic BTO by replacing Ti with Fe [20-27] and Co [28-31]. Maier *et al.* were the first to show ferroelectricity and ferrimagnetism [20] in Fe-doped BTO. More recently, Rajamani *et al.* [21] and Xu *et al.* [24] showed ferromagnetism at room temperature in Fe-doped BTO samples. For Co-doped BTO, ferromagnetism at room temperature was shown by Lee *et al.* [29] and Lin *et al.* [30], but the existence of ferroelectricity in their samples was not addressed.

In this work, we demonstrate the epitaxial integration of Co-substituted BTO grown by molecular beam epitaxy (MBE) on Ge (001) substrates. Ferroelectricity is exhibited by a 5% Co-substituted BTO film, but no sign of magnetic ordering is observed, independent of Co concentration up to 40%. First-principles calculations are performed to investigate the role of oxygen vacancies in the magnetic ordering in $BaTi_{1-x}Co_xO_3$ (BTCO). The results suggest that the presence of oxygen vacancies in BTCO can quench ferromagnetism by creating locally antiferromagnetically coupled pairs of Co atoms that exhibit no net magnetic moment.

II. Experiment

In this study, Ga-doped germanium (001) wafers (0.019 Ω-cm) that are diced into 10 × 10 mm^2 squares, and 5 × 5 mm^2 square single crystalline $SrTiO_3$ (001), are used as substrates. The $SrTiO_3$ substrates are degreased with acetone, isopropyl alcohol (IPA) and de-ionized water (18.2 MΩ-cm) in a sonicator for 10 minutes, followed by vacuum anneal at 750°C for 15 min prior to deposition. The Ge substrates are cleaned using a combination of regular degreasing in acetone, IPA and de-ionized water in a sonicator for 10 min each, followed by *in situ* exposure to oxygen plasma for 30 min and a subsequent anneal, leading to an atomically flat, 2 × 1

reconstructed and contamination-free surface. The details of the Ge cleaning process are given elsewhere [32]. Annealing and growth of the samples are performed in a customized DCA Instruments M600 MBE chamber. Effusion cells are utilized for Sr, Ti and Ba deposition while electron beam evaporation is used for Co. A quartz crystal microbalance is used to calibrate the fluxes.

Prior to film growth on Ge, a ½ monolayer of barium metal is deposited on the clean Ge (001) surface at 200°C. This Zintl template prevents Ge from oxidizing during subsequent growth in an oxygen atmosphere. Five unit cells of amorphous strontium titanate (STO) are deposited at 200°C on the Zintl template, in an environment of 5×10^{-7} torr of molecular oxygen. The STO layer is crystallized by annealing the sample to 750°C with a ramp rate of 30°C/min. On top of the crystallized STO buffer layer, two unit cells of undoped BTO are first deposited prior to depositing $BaTi_{1-x}Co_xO_3$ (BTCO), where *x* denotes the Co concentration. To study the effect of Co concentration, samples are grown with Co concentrations in the range of x = 2 - 40%. Both undoped and Co-doped BTO films are deposited at 5×10^{-6} torr of molecular oxygen at 750°C with a growth rate of 1 unit cell per 2 minutes, and are crystalline as deposited. Samples with thicknesses ranging from 10 to 16 nm are grown and then cooled down to 200°C with a ramp rate of 30°C/min in an oxygen environment of 5×10^{-6} torr. During growth, reflection-high-energy electron diffraction (RHEED) with 21 keV electrons at a grazing angle of 3° is used to monitor the quality and crystallinity of the samples. Immediately after deposition, the samples are transferred *in situ* to an X-ray photoelectron spectroscopy (XPS) system allowing XPS measurements without breaking vacuum. The XPS analysis chamber is equipped with a VG Scienta R3000 electron analyzer and a monochromatic Al Kα radiation (hν = 1486.6 eV) source with the x-rays incident at 54.7° from normal. The analyzer is calibrated using a clean silver foil such that the Ag $3d_{5/2}$ binding energy is 368.28 eV. To determine the lattice constants of our samples, X-ray diffraction measurements of the BTCO films are carried out, using a Phillips XPERT Theta-Theta diffractometer with a Cu Kα radiation source. For determining the Co concentration, Rutherford backscattering spectroscopy (RBS) measurements are performed on selected samples with He^+ ions at 2.3 MeV using an NEC 3UH Pelletron. Cross-sectional transmission electron microscopy (TEM) is carried out on a sample with 25% Co using a JEOL 4000EX operated at 400 kV and a JEOL 2010F operated at 200 kV. For the energy-dispersive X-ray spectroscopy (EDXS) line profile, the JEOL 2010F is used with an energy dispersion of 10 eV per channel and 1 nm probe size. Scan time for each point lies between 20 and 30 seconds. Electron energy-loss spectroscopy (EELS) measurements are performed on a Nion UltraSTEM 100 operated at 60 keV. Band-Excitation (BE) PFM and voltage spectroscopy are performed on a commercially available Asylum AFM platform (Cypher instrument) using PXI-based National Instruments data acquisition cards and in-house software at CNMS, ORNL. The BE-Piezoresponse Spectroscopy (BEPS) measurements are all carried out in the off-field state and at room temperature. Magnetization vs. magnetic field measurements are performed on a Quantum Design Magnetic Property Measurement System apparatus. Measurements are made at 5 K in a magnetic field ranging from ±5 kOe. Field-cooled and zero-field-cooled magnetization vs.

temperature scans are also carried out from 300 K to 5 K in 2 K increments under an applied field of 200 Oe. A commercial Veeco MultiMode V atomic force microscope (AFM) with a commercially available magnetic force microscopy (MFM) tip in lift mode is used to simultaneously image local topographic and magnetic contrast of the BTCO surface.

III. Computational details

First-principles calculations are performed using the Vienna *ab initio* simulation package (VASP) [33]. Projector-augmented wave pseudopotentials [34, 35] utilizing the local density approximation of Perdew and Zunger [36] are used to describe each atomic species. The chosen valence configurations are $4s^2 4p^6 5s^2$ for Ba, $3s^2 3p^6 4s^1 3d^1$ for Ti, $3d^8 4s^1$ for Co, and $2s^2 2p^4$ for O. In order to account for the electronic correlation effects of the $3d$ states for the Co atom, calculations are performed using the L(S)DA+U approach of Dudarev, *et al.* [37] utilizing a U_{eff} of 4.0 eV, consistent with previous calculations and the spin state of Co^{4+} in $SrCoO_3$ [38-40]. The calculations employ a plane-wave cutoff energy of 600 eV and the Brillouin zone is sampled using a Γ-centered Monkhort-Pack grid [41] of 12 × 12 × 12 for the primitive cell. Relaxations are performed with a threshold of 10^{-2} eV/Å and integration of the Brillouin zone for self-consistent total energy calculations is performed using the tetrahedron method with Blöchl corrections [42]. Incorporation of both Co and oxygen vacancies are performed using a variety of supercell configurations in which at least one primitive cell of BTO is always included to separate the repeated image of the defect. In these cases, appropriately scaled k-point grids are used and all atomic coordinates are allowed to relax (with the lattice constants fixed to the theoretical values for nominal BTO).

IV. Results and discussion

A. RHEED

Growing undoped BTO directly on Ge results in in-plane polarized BTO due to the lack of sufficient compressive strain to overcome thermal expansion mismatch between the film and substrate [43]. A thin layer of 2-nm-thick STO grown between the Ge substrate and BTO imposes compressive strain on the BTO film leading to out-of-plane polarization of the BTO film [44]. Growing two unit cells of undoped BTO on top of STO before growing BTCO improves crystallization of the BTCO layer. The crystalline quality of the BTCO samples appear to be highly sensitive to the actual metal flux ratios, as small variations from ideal stoichiometry lead to poor crystalline quality or even polycrystalline films. RHEED patterns of BTCO films grown on an STO(001) substrate with different Co concentrations are shown in Figure 1. At Co concentrations between 15 - 25%, sharp and very streaky patterns are visible, indicative of a highly ordered surface. Increasing the Co concentration in the BTCO films up to 30 - 40% leads to broader streaks, indicating a rougher surface and more crystalline disorder. For most samples,

no additional diffraction spots are visible in the RHEED patterns during and after growth, confirming the absence of Co clusters or secondary phases. Additional spots are detected only in rare cases, which usually result from non-stoichiometric BTCO due to either excess Ti or Co. Only films that show good crystallinity are considered for subsequent characterization.

B. X-ray photoemission spectroscopy

To quantify the Co concentration of the BTCO films, *in situ* XPS measurements are carried out immediately after growth. Due to the overlap of the Co $2p_{3/2}$ peak at 780 eV with the much stronger Ba $3d_{5/2}$ peak at the same binding energy, XPS analysis of BTCO films cannot easily be used for stoichiometry determination [45]. Since Co is only present in relatively small concentrations, other Co signals including Co Auger peaks are usually buried in the background and are too weak to be used for reliable analysis. For this reason, two different techniques are used to estimate the Co concentrations. First, Rutherford backscattering spectroscopy (RBS) is performed on two different samples with nominal Co concentrations of 5 and 10% to confirm the accuracy of the assumed Co concentrations based on measured flux ratios. For the BTCO film with nominally 5% Co, a concentration of 7.3 ± 3.7% is measured. The nominally 10% Co-substituted sample exhibits 6.9 ± 3.9% Co. Both measurements indicate rough agreement with the nominal Co concentrations. The reason for the large error bars in RBS can be explained by the low Co concentrations, and in addition, the small layer thicknesses also contribute to the uncertainty. The second technique is an indirect method using XPS to measure the Co concentrations. Right after growth of a BTCO sample, a $SrTi_{1-x}Co_xO_3$ (STCO) film is grown on another Ge substrate, with the same growth conditions, Co concentration and film thickness as the previous BTCO film. For these STCO films, XPS measurements can be used for determining the Co concentration since the Sr core levels do not overlap with the Co 2*p* peaks. The evaluation of the XPS spectra reveals that these STCO samples show good agreement with the nominal Co concentration. However, due to the high signal to noise ratio and weak intensity of the Co 2*p* spectra, peak fitting is not unambiguous. Based on the STCO XPS data, an absolute error of ±2.0% for the Co concentration in the grown BTCO samples is assumed.

XPS can also be used to determine the relative change in the oxygen content between BTCO and undoped BTO films. To do this, we measure Ba 4*d* and O 1*s* peaks in the BTCO films and in undoped BTO films for comparison. Doped and equivalent undoped samples are grown under the same growth conditions and have the same thickness. The area ratio of the O 1*s* and Ba 4*d* peaks in both samples can then be used to determine the change in oxygen content in the BTCO films and subsequently extract an estimate of their oxygen vacancy concentrations. In a previous study of MBE-grown $SrTi_{1-x}Co_xO_3$ on Si by Posadas *et al.* [38], it was shown that the oxygen vacancy concentration correlates roughly with the amount of Co substitution in the STCO samples, indicating that Co doping promotes the formation of oxygen vacancies. Similar results are found for the grown BTCO films. For samples grown with Co concentrations between 5 - 15%, the amount of oxygen vacancies correlates roughly with the amount of Co, which is in good agreement with the previous result [38]. However, a somewhat different behavior is

observed for higher Co concentrations in BTO. Only 20.8% oxygen vacancies are found for a nominally 30% Co-substituted BTCO film, while the amount of oxygen vacancies is determined to be as low as 26.4% for a nominally 40% Co-substituted sample. The role and importance of these oxygen vacancies on the magnetic ordering of BTCO is explained in detail in section V.

C. X-ray diffraction

To further characterize the BTCO films, X-ray diffraction (XRD) is used to determine in-plane and out-of-plane lattice constants and overall crystalline quality. Figure 2 shows a symmetric 2θ-θ scan of a 10-nm-thick BTCO film with a Co concentration of 5% grown on an STO/Ge template. The high-resolution scan around the BTCO (002) peak gives an out-of-plane lattice constant of 4.06 Å. Rocking curve scans around the BTCO (002) peak for films grown on Ge typically show a full-width at half maximum (FWHM) of 0.8 - 1.4° whereas BTCO films grown on an STO single crystal substrate show a FWHM of 0.08 - 0.20°. Only peaks from Ge, STO and a single orientation of the BTCO film are observed. The expanded out-of-plane lattice constant indicates an out-of-plane orientation of the polarization of the BTCO films. Out-of-plane lattice constant measurements for BTCO samples with Co concentrations ranging from 2 - 40% all show lattice constants in the range of 4.03 - 4.06 Å with no obvious trend with respect to Co concentration. No secondary phases are detectable (e.g. CoO at $2\theta \sim 42°$), indicative of uniform Co distribution.

It was shown by several groups [46-49] that an antiferromagnetic hexagonal phase of Co-doped BTO powder samples can be stabilized at room temperature. To rule out a potential hexagonal phase of BTCO, measurements around the expected position of the $(317)_{hex}$ reciprocal lattice point of a 25% Co-doped BTO sample are carried out. This plane is only present for the hexagonal BTCO crystal structure and differentiates it from the perovskite structure. The absence of this plane spacing lead us believe that our BTCO films are in the perovskite structure and not in the hexagonal phase, even for high Co concentrations. Additionally, grazing incidence $2\theta_\chi$–ϕ in-plane diffraction measurements confirm a square in-plane symmetry, which underlines our observation that our BTCO films grow with the perovskite crystal structure and with no other phases present.

D. Electron microscopy

To confirm the crystal quality and uniform distribution of Co atoms in the BTCO films, cross-sectional high-angle annular-dark field (HAADF) TEM measurements are carried out. Figure 3a) shows a HAADF image of a 12-nm-thick 25% Co-substituted BTCO film on 2-nm-thick STO on Ge. High crystallinity of the BTCO layer and the STO buffer, as well as sharp interfaces between the layers without visible interdiffusion, is confirmed. No signs of Co clustering or CoO precipitates can be observed in the BTCO layer even for low magnification imaging. To further investigate the distribution of Co within the sample, EDXS measurements are performed parallel to the Ge surface in the BTCO film. As can be seen in Figure 3b), the Co atoms are uniformly

distributed within the sample with only statistically insignificant fluctuations. Layer-resolved EELS measurements, which are performed on the same sample, reveal that the oxidation state of the Ti atoms changes within the film (Figure 3c, d). Ti atoms close to the Ge interface exhibit an oxidation state of +4 as can be seen by the splitting of the Ti L-edge. However, the split gradually weakens closer to the surface, indicating the presence of Ti atoms with an oxidation state of +3. This Ti reduction is an artifact attributed to argon-ion milling during the TEM sample preparation process, because only regions close to the surface are affected by it and XPS measurements, which were carried out immediately after growth, indicate no Ti^{3+} signal of the grown $BaTi_{1-x}Co_xO_{3-\delta}$ films independent of the Co concentration.

E. Piezo force microscopy

The ferroelectric properties of the BTCO samples are evaluated using Band-Excitation Piezoresponse Force Microscope (BE-PFM). A BTCO sample with a Co concentration of 5% is used to demonstrate ferroelectricity. A typical result of a box-in-box switching experiment is shown in Figure 4a). An area of 5 × 5 μm^2 is initially poled with a tip held at -5 V while a smaller square of 2.5 × 2.5 μm^2 within the bigger square is poled with a tip held at +5 V. Clear switching is observed and the vertical BE-PFM amplitude and phase (Figure 4b, c) show clear and sharp boundaries indicating ferroelectric domains.

In conjunction with the BE-PFM tests, BEPS measurements are carried out on the same sample. 100 hysteresis loops across a 10 × 10 grid are measured and the average amplitude and phase response of the acquired loops are shown in Figure 4d, e). The amplitude curve exhibits a butterfly-like hysteresis which is characteristic for ferroelectric materials. The phase loop, however, appears to have a change somewhat less than 180°. However, there is significant variability in the switching behavior on the sample surface, and some points do not appear to switch well. This may be indicative of electrochemical phenomena in addition to the ferroelectric processes, high leakage current (that is spatially variable, e.g. due to defects), or both.

F. Magnetic measurements

To determine if the BTCO films are magnetic, superconducting quantum interference device (SQUID) and MFM measurements are performed. For SQUID measurements, BTCO films are grown on single crystal STO substrates to facilitate crystallization of the BTCO layer. For magnetization vs. field and magnetization vs. temperature measurements, the background signal of the STO substrate is subtracted by measuring the specific substrate separately, immediately before growth of the BTCO layer.

The magnetization vs. field and magnetization vs. temperature behavior of several BTCO samples with different Co concentrations (5, 10, 20, 25%) are measured. However, after subtracting the background signal of the STO substrate, the magnetization vs. field

measurements show no sign of ferromagnetism. A hysteresis curve, typical for ferromagnetism, is not observed for any samples, independent of the Co concentration (see Figure 5 for a 25% Co-substituted 16-nm-thick BTCO film), with only very weak paramagnetism in some samples. When performing magnetization vs. temperature measurements, a rather unusual behavior is obtained, as the magnetization showed a slight decrease with temperature throughout the cooling process from 300 to 5 K, without any jumps or other anomalies.

For room temperature MFM measurements, two 16-nm-thick BTCO samples on an STO/Ge template with 15 and 30% Co concentration, respectively, are scanned to detect any signals of magnetic moments on the surfaces of the BTCO films. For both samples, low surface roughness is confirmed. For the 30% Co-substituted BTCO sample, a surface roughness between 0.65 and 1.3 nm is measured, depending on the scanned area, while a RMS of only 0.25 nm is detected for the 15% Co-substituted sample. In both cases, the lack of magnetic contrast in the frequency shift images is very clear, indicating that the samples are either non-magnetic or the magnetic signal is not detectable within the limits of the MFM. The apparent absence of magnetism is in agreement with the SQUID measurements, which also did not reveal any sign of ferromagnetism.

G. Theoretical modeling

Theoretical modeling was performed in order to shed light on the experimental lack of detectable magnetism or even paramagnetic response despite the presence of cobalt in the film. Depending upon the oxygen vacancy ratio, cobalt can be in the Co^{4+} state (no vacancies), Co^{3+} state (a $\frac{1}{2}$ of an oxygen vacancy per cobalt), or Co^{2+} state (one oxygen vacancy per cobalt). In the following section, we explore each spin state in an effort to provide a possible explanation for the lack of observed magnetic signature when oxygen vacancies are included in either ratio.

For undoped BTO, lattice constants of a = 3.945 Å and c = 3.989 Å (c/a ratio of 1.011) are obtained, consistent with experimental values of a = 3.990 Å, $\frac{c}{a}$ = 1.011 [50]. In order to model Co-doped BTO, we first consider a single Co atom replacing a titanium atom in a 2 × 2 × 2 supercell. In a tetragonal crystal like BTO, there is an elongation of the octahedral complex which can lead to further breaking of the *d*-state degeneracy from the usual t_{2g} and e_g states into e_g, b_{2g}, a_{1g}, and b_{1g} states. Therefore, for a Co^{4+} ion with five electrons, there are three possible spin-states: low spin ($\mu = 1\ \mu_B$), intermediate spin ($\mu = 3\ \mu_B$), and high spin ($\mu = 5\ \mu_B$). It is also possible that hybridization can suppress any magnetic moment, as has been reported for Co-doped cubic BTO [51, 52]. Our calculations show that the low-spin state is the ground state for Co-doped BTO in the absence of oxygen vacancies (favored by 6 meV relative to the intermediate-spin state, 162 meV relative to the non-spin-polarized state, and 180 meV relative to the high-spin state). For the low-spin state, the total cell moment is 1.00 μ_B with 0.96 μ_B locally on the Co atom and the system is insulating, with the occupied Co states hybridized at the

bottom of the O-2*p* band and a reduced gap (compared to undoped BTO) due to the presence of the unoccupied Co states just below the bulk Ti 3*d* derived conduction band.

We next consider the inclusion of two neighboring Co atoms oriented either parallel (apical) or perpendicular (basal) to the tetragonal axis using 2 × 2 × 3 and 3 × 2 × 2 supercells, respectively. In the nearest neighbor configuration, the Co atoms prefer the intermediate-spin state. For the apical pair, ferromagnetic coupling is preferred and while the total cell magnetic moment is 6.00 μ_B, individually the Co atoms have slightly differing moments of μ_{Co} = 2.24 μ_B and μ_{Co} = 2.61 μ_B. It should be noted that this is not a "mixed spin" state as the (higher in energy) ferromagnetic high-spin state can be stabilized with μ_{total} = 10.00 μ_B and the high-spin local moment is calculated to be μ_{Co} = 3.17 μ_B. Furthermore, the antiparallel arrangement is actually a two-site antiferrimagnetic state with a total moment of $|\mu_{total}|$ = 0.60 μ_B and is 16 meV higher in energy. Similarly, the basal pair favors an intermediate spin state with μ_{total} = 6.02 μ_B and again has slightly differing moments of μ_{Co} = 2.20 μ_B and μ_{Co} = 2.76 μ_B. As in the apical case, the differing moments lead to an antiparallel arrangement that is higher in energy (ΔE = 44 meV) and a non-zero total moment ($|\mu_{total}|$ = 1.04 μ_B). Overall, the basal ferromagnetic arrangement is lowest in energy; its density of states is shown in Figure 6. As for the single Co case, the occupied Co states are partially hybridized with the lower portion of the oxygen 2*p* states. More states are present in this region than before due to the increased spin moment, and hybridization pushes the top of the majority spin channel oxygen bands above the Fermi energy making the system metallic. In fact, all four of the above described states are metallic in nature (i.e. non-zero density of states at the Fermi energy) as opposed to the single Co atom case. Furthermore, in comparison to the dilute limit (i.e. isolated cobalt substitution), clustering of cobalt is preferred.

The experimental data shows vacancy concentrations ranging from approximately one oxygen vacancy for every two Co atoms (Co^{3+}) to one oxygen vacancy for every Co atom (Co^{2+}). Furthermore, the above results imply that in the absence of oxygen vacancy, there should be a detectable magnetic signal and that the material would be metallic for clustered Co. Therefore, calculations are performed for the two primary ratios of oxygen vacancies to Co atoms in order to provide a better comparison.

In order to simulate Co^{3+}, we require a simulation cell containing two Co atoms and a single oxygen vacancy. A defect arrangement for transition metal impurity atoms resulting in the 3+ state is for two impurity atoms to occupy neighboring sites with an oxygen vacancy situated in between. Such a defect structure has been confirmed using experimental and theoretical techniques, for example for Fe^{3+} in $SrTiO_3$ [53]. It is also similar to the observance of linearly oriented clustered defects in Co:$SrTiO_3$ [39] and consistent with clustering of Co. Therefore, this defect is considered as the most plausible for the one vacancy per two Co dopant atoms, and we construct such a defect aligned as both an apical defect (a 2 × 2 × 3 supercell) and a basal defect (a 3 × 2 × 2 supercell). The later is shown in Figure 7. A Co atom in the Co^{3+} state has six

electrons which implies that for the tetragonally distorted octahedral crystal field, the Co can have low-spin ($\mu = 0\ \mu_B$), intermediate-spin ($\mu = 2\ \mu_B$), or high-spin ($\mu = 4\ \mu_B$) configurations. For both geometric orientations, the lowest energy spin configuration is an antiferromagnetic high-spin configuration (locally $|\mu_{Co}| = 2.96\ \mu_B$) with the basal plane defect having the lowest energy of the considered geometrical configurations. The difference in energy for the antiferromagnetic and ferromagnetic arrangements is 23 meV and 29 meV for basal and apical defects, respectively. As shown in Figure 7, the density of states shows the occupied Co *d*-states either below the oxygen 2*p* states in energy or hybridized at the bottom of the oxygen 2*p* bands. The unoccupied Co *d*-states sit just below the nominal conduction band implying that the material is an insulator with a reduced gap compared to undoped BTO. The ferroelectric distortion (as indicated by the relative distortion of Ti and O atoms along the c-axis) is maintained for this configuration with a small reduction for the Ti atoms (and oxygen in between) that sit immediately over the Co atoms. In comparison, the low spin Co^{3+} state, which would also have explained the lack of magnetic moment, is found to be significantly higher in energy (590 meV) than the low energy antiparallel high spin state.

For a one-to-one ratio, we expect a Co^{2+} oxidation state which has seven electrons and can thus be in either a low-spin ($\mu = 1\ \mu_B$) or high-spin ($\mu = 3\ \mu_B$) state. Furthermore, due to the tetragonal symmetry of the cell, the oxygen vacancy (similar to the case of two Co atoms) can be created at an oxygen site parallel to the tetragonal axis (apical) or perpendicular (basal). For the calculation of this ratio, a $2 \times 2 \times 2$ supercell is used for the apical vacancy neighboring the Co atom. Energetically, the vacancy prefers to form at a site neighboring the Co dopant atom. In all cases, the high-spin state is favorable with the apical complex lowest in energy. Locally, the Co atom has a magnetic moment of 2.60 μ_B, while the total cell moment is 3.00 μ_B. Such a defect is insulating with the majority spin Co states hybridized at the bottom oxygen 2*p* band and the minority spin Co states hybrized at the top of the oxygen 2*p* band. The unoccupied Co states overlap with the Ti states in the conduction band.

Given that two Co atoms with a single oxygen vacancy in between display antiferromagnetic coupling, we next consider a neighboring pair of Co-vacancy complexes. Essentially, the considered structure can be described as adding an additional oxygen vacancy to the two Co/one oxygen vacancy configuration described earlier, with this additional vacancy either along the same axis as the previous defect or perpendicular to it. Therefore, as in the case of the 2 Co/1 V_O case, we use $2 \times 2 \times 3$ and $3 \times 2 \times 2$ supercells. Of the five symmetrically distinct configurations possible for such a defect, the arrangement with a basal Co pair and oxygen vacancy and an additional perpendicular, apical vacancy has the lowest energy (see Figure 8 for the structure). Such a defect stabilizes as an antiferromagnetically coupled high-spin state with the ferromagnetic arrangement being 8 meV higher in energy. The AFM configuration has a calculated $\mu_{total} = 0.00\ \mu_B$ and local moments of $\mu_{Co} = 2.61\ \mu_B$ and $\mu_{Co} = -2.52\ \mu_B$ (the slight discrepancy is due to excess magnetization on neighboring oxygen). Similar to a single Co-V_O

complex, placing two such complexes at neighboring sites leads to an insulating material. Here the spin majority and spin minority channels mirror each other approximately. The reason the states do not line up exactly is that the specific energy levels of the orbitals are shifted slightly due to distortions caused by the local geometry of the two Co atoms being slightly different. The two Co/two oxygen vacancy complex, unlike a single pair, supports the experimental result of a simultaneous non-magnetic and insulating film with Co.

In order to understand why no magnetism (including a noticeable paramagnetic signal) is detected at the field strengths considered in the magnetic measurements, we use an effective Heisenberg Hamiltonian which includes the Heisenberg term (H_H) and Zeeman term (H_Z):

$$H = H_H + H_Z = -2\sum_{i<j} J_{ij}\hat{S}_i \cdot \hat{S}_j - g\mu_B H_0 \sum_i S_{iz}\,, \qquad (1)$$

where $\hat{S}_i$ is the electronic spin of the given site, J_{ij} the coupling strength between spins, g is the electron spin g-factor, μ_B is the Bohr magneton, and H_0 the applied magnetic field. Since density functional theory is a 0 K theory and the measurements are taken at low temperature, we can safely ignore temperature effects. By expanding the Hamiltonian given in Eq. (1) for both the case of two locally ferromagnetic spins and two locally antiferromagnetic spins, the field strength at which the parallel alignment is favored over anti-parallel alignment can be determined as:

$$H_0 \geq -\frac{\Delta E}{2g\mu_B S}\,, \qquad (2)$$

where $\Delta E = E_{AFM} - E_{FM}$ and can be related to the spin coupling strength J. Of the reported configurations, the smallest ΔE occurs for the described lowest-energy two-vacancy/two-Co. For this configuration, $\Delta E = 8$ meV and $S = \frac{3}{2}$ which implies that a magnetic field strength of $H_0 = 23$ T would be needed to overcome the coupling, significantly above that used for the SQUID measurements. In the case of the locally antiferromagnetic, high-spin Co^{3+}, the field strength would be even higher due to the previously mentioned increased ΔE. Furthermore, since the thermal energy at 300 K is 25.8 meV, such a configuration for Co^{3+} would not be detected in the magnetization vs temperature sweeps.

H. Discussion

For ferroelectric materials, it is known that the introduction of sufficient oxygen vacancies results in the disappearance of the polarization and the lowering of the Curie temperature [54]. For that reason the amount and distribution of oxygen vacancies in our $BaTi_{0.95}Co_{0.05}O_3$ film is essential to understand the existence of ferroelectricity. Our XRD and RHEED measurements, as well as cross-sectional TEM images, show the absence of phase segregations or clustering of Co atoms in our BTCO films independent of the Co concentration. As a matter fact, EDXS measurements indicate a uniform distribution of Co atoms in our films. This is in accordance

with the PFM measurements which reveal that there is no substantial phase segregation within the resolution limit of the instrument. Additionally, the detection of a magnetic signal would be likely if Co clusters had formed. Theoretical calculations of Fe-doped $SrTiO_3$ [53] and Co-doped $BaTiO_3$ [55] show that the TM-V_O-TM complex is the preferred structure. Based on these findings, we assume that the oxygen vacancies prefer to form next to Co atoms and are not randomly distributed throughout the film. However, due to the small amount of induced oxygen vacancies in a 5% Co doped BTCO film, the polarization of $BaTiO_3$ is only expected to be attenuated and not completely suppressed with respect to undoped $BaTiO_3$.

Our experimental and theoretical results also indicate that the Co-V_O complex plays a crucial role in the formation of magnetic ordering in Co-substituted metal oxide films, which has been already shown for Co:STO (STCO) by Florez *et al.* [56] and Posadas *et al.* [38] as well as for Co:TiO_2 by Roberts *et al.* [57]. In agreement with these studies, we show that the partial substitution of Co atoms facilitates the formation of oxygen vacancies in their close proximity, leading to Co-V_O pairs. From DFT calculations, in the case where there are no oxygen vacancies, which imparts Co with a valence state of 4+, the results for STCO and BTCO are very similar. Co stabilizes in the low spin state and interacts ferromagnetically with adjacent Co atoms but the interaction is very short range. However, Posadas *et al.* showed that if oxygen vacancies are present in STCO with a concentration equal to the Co concentration, then Co stabilizes in the 2+ valence state. They showed theoretically that the Co(II)/V_O complex is responsible for the ferromagnetic and insulating behavior of their films. Interestingly, the ferromagnetic behavior due to the 2Co/2V_O complex, which is present in STCO, is not observed for BTCO films. Even though we also observe a correlation between the Co concentration and the amount of oxygen vacancies formed in BTCO similar to the case of STCO, the presence of oxygen vacancies in BTCO leads to an antiferromagnetic ordering instead. This lack of a magnetic moment is confirmed by both SQUID and MFM measurements. The numerical estimate of the magnetic field strength needed to overcome the antiferromagnetic ordering confirms our observations of the absence of any magnetic signal in BTCO films.

The finding of a lack of magnetism in BTCO films is contrary to reports by Lin *et al.* [30] and Lee *et al.* [29], which both observed ferromagnetism in Co-substituted BTO films. Lin *et al.* used pulsed laser deposition (PLD) to deposit $BaTi_{0.95}Co_{0.05}O_3$ thin films of various thicknesses on Nb:STO substrates and found that the Co atoms are in a 3+ valence state. Lee *et al.* used ion implantation to create 3 and 5% Co-substituted BTO layers which showed ferromagnetic behavior. Similar to our study, both groups report the absence of Co clusters using XRD and TEM. However, both PLD growth and ion implantation, being far from equilibrium processes, are prone to forming nanoscale clusters that could be small enough to be measured by a SQUID magnetometer but without being detectable in XRD. In both studies the presence of oxygen vacancies was not investigated, despite the assumption by Lin *et al.* to be the origin of ferromagnetism in their films. In the case of Co:TiO_2 [57] that was grown by rf-magnetron sputter deposition at 4×10^{-3} torr, it was shown that a vacuum anneal promotes the formation of

oxygen vacancies. Since PLD and ion implantation operate under similar pressures between 10^{-1}-10^{-5} torr, it is possible that at these higher pressures, the formation of oxygen vacancies in BTCO is suppressed. The lack of vacancies in these ferromagnetic BTCO films would be consistent with our theoretical results, which predict ferromagnetism in fully oxidized BTCO films.

V. Conclusions

In summary, we have investigated ferroic order in Co-substituted BTO films grown on Ge(001) and STO(001) substrates by MBE. XPS measurements show that the formation of oxygen vacancies depends on the Co-concentration in the sample. The existence of ferroelectricity of a 5% Co-substituted BTCO film is confirmed using PFM. However, SQUID and MFM measurements show no sign of magnetism, including paramagnetism, for any Co concentration. First-principles calculations demonstrate that while BTCO would exhibit a net moment in the absence of oxygen vacancies, the observed lack of detectable moments in the presence of oxygen vacancies may be due to Co and oxygen vacancies forming defect complexes that are locally antiferromagnetic. The field required to overcome this antiferromagnetism is on the order of 20 T. Furthermore, calculations of these low energy defects show them to be insulating and ferroelectric in agreement with experiment.

Acknowledgments

This work was supported by the Air Force Office of Scientific Research under grant FA9550-12-10494 and Texas Advanced Computing Center. HXC thanks the National Natural Science Foundation of China for supporting her stay at the University of Texas at Austin under grant No. 11104194. A portion of this research was sponsored by the Division of Materials Sciences and Engineering, BES, DOE (RKV, SVK). Research was conducted at the Center for Nanophase Materials Sciences, which is a DOE Office of Science User Facility with support from MBO and SJ.

References:

[1] W. Eerenstein, N. D. Mathur, J. F. Scott, Nature **442**, 759-765 (2006)

[2] H. Béa, M. Gajek, M. Bibes, A. Barthélémy, J. Phys.: Condens. Matter **20**, 434221 (2008)

[3] M. Bibes, A. Barthélémy, Nature Mater.**7**, 425 426 (2008)

[4] M. Bibes, J. E. Villlegas, A. Barthélémy, Adv. Phys. **60**, 5 84 (2011)

[5] M. Gajek, M. Bibes, S. Fusil, K. Bouzehouane, J. Fontcuberta, A. Barthélémy, A. Fert, Nature Mater. **6**, 296 302 (2007)

[6] Z. Yan, Y. Guo, G. Zhang, J.M. Liu, Adv. Mater. **23**, 1351 (2011)

[7] N. A. Hill, J. Phys. Chem. B **104**, 6694–6709 (2000)

[8] H. Schmid, Ferroelectrics **162,** 317–338 (1994)

[9] S. W. Cheong, M. Mostovoy, Nature Mater. **6**, 13 (2007)

[10] R. Ramesh, N. A. Spaldin, Nature Mater. **6**, 21 (2007)

[11] W. Prellier, M. P. Singh, P. Murugavel, J. Phys.: Condens. Matter **17**, 803-832 (2005)

[12] T. Katsufuji, S. Mori, M. Masaki, Y. Moritomo, N. Yamamoto, H. Takagi, Phys. Rev. B **64**, 104419 (2001)

[13] T. Kimura, S. Kawamoto, I. Yamada, M. Azuma, M. Takano, Y. Tokura, Phys. Rev. B **67**, 180401 (2003)

[14] J. Wang, J. B. Neaton, H. Zheng, V. Nagarajan, S. B. Ogale, B. Liu, D. Viehland, V. Vaithyanathan, D. G. Schlom, U. V. Waghmare, N. A. Spaldin, K. M. Rabe, M. Wuttig, R. Ramesh, Science **299**, 1719-1722 (2003)

[15] A. Moreira dos Santos, S. Parashar, A. R. Raju, Y. S. Zhao, A. K. Cheetham, C. N. R. Rao, Solid State Commun. **122**, 49-52 (2002)

[16] X. H. Zhu, H. Béa, M. Bibes, S. Fusil, K. Bouzehouane, E. Jacquet, A. Barthélémy, D. Lebeugle, M. Viret, and D. Colson, Appl. Phys. Lett. 93, 082902 (2008)

[17] H. Nakayama, H. Katayama-Yoshida, Jpn. J. Appl. Phys. **40**, 1355-1358 (2001)

[18] H. K. Chandra, K. Gupta, A. K. Nandy, P. Mahadevan, Phys. Rev. B **87**, 214110 (2013)

[19] V. Sharma, G. Pilania, G. A. Rossetti Jr., K. Slenes, R. Ramprasad, Phys. Rev. B **87**, 134109 (2013)

[20] R. Maier, J. L. Cohn, Appl. Phys. Lett. **78**, 2536-2538 (2001)

[21] A. Rajamani, G. F. Dionne, D. Bono, C. A. Ross, J. Appl. Phys. **98**, 063907 (2005)

[22] S. Ray, P. Mahadevan, S. Mandal, S. R. Krishnakumar, C. S. Kuroda, T. Sasaki, T. Taniyama, M. Itoh, Phys. Rev. B **77**, 104416 (2008)

[23] F. Lin, D. Jiang, X. Ma, W. Shi, J. Magn. Magn. Mater. **320**, 691-694 (2008)

[24] B. Xu, K. B. Yin, J. Lin, Y. D. Xia, X. G. Wan, J. Yin, X. J. Bai, J. Du, Z. G. Liu, Phys. Rev. B **79**, 134109 (2009)

[25] Z. Chao, C. L. Wang, J. C. Li, K. Yang, Chin. Phys. **16**, 1422 (2007)

[26] E. V. Ramana, S. M. Yang, R. Jung, M. H. Jung, B. W. Lee, C. U. Jung, J. Appl. Phys. **113**, 187219 (2013)

[27] A. Zorko, M. Pregelj, M. Gomilsek, Z. Jaglicic, D. Pajic, M. Telling, I. Arcon, I. Mukulska, M. Valant, Scientific Reports **5**, 7703 (2015)

[28] S. Ray, Y. V. Kolen'ko, K. A. Kovnir, O. I. Lebedev, S. Turner, T. Chakraborty, R. Erni, T. Watanabe, G. van Tendeloo, M. Yoshimura, M. Itoh, Nanotechnology **23**, 025702 (2012)

[29] J. S. Lee, Z. G. Khim, Y. D. Park, D. P. Norton, N. A. Theodoropoulou, A. F. Hebard, J. D. Budai, L. A. Boatner, S. J. Pearton, R. G. Wilson, Solid State Electron. **47**, 2225-2230 (2003)

[30] Y.-H. Lin, S. Zhang, C. Deng, Y. Zhang, X. Wang, C.W. Nan, Appl. Phys. Lett. **92**, 112501 (2008)

[31] L. B. Luo, Y. G. Zhao, H. F. Tian, J. J. Yang, H. Y. Zhang, J. Q. Li, J. J. Ding, B. He, S. Q. Wei, C. Gao, Appl. Phys. Lett. **92**, 232507 (2008)

[32] P. Ponath, A. Posadas, R. Hatch, A. A. Demkov, J. Vac. Sci. Technol. B **31**, 031201 (2013)

[33] G. Kresse and J. Furthmüller, Phys. Rev. B **54**, 11169 (1996)

[34] P. Blöchl, Phys. Rev. B **50**, 17953 (1994)

[35] G. Kresse, D. Joubert, Phys. Rev. B **59**, 1758 (1999)

[36] J. Perdew, A. Zunger, Phys. Rev. B **23**, 5048 (1981)

[37] S. Dudarev, G. Botton, Phys. Rev. B **57**, 1505 (1998)

[38] A. B. Posadas, C. Mitra, C. Lin, A. Dhamdhere, D. J. Smith, M. Tsoi, A. A. Demkov, Phys. Rev. B **87**, 144422 (2013)

[39] C. Mitra, C. Lin, A. B. Posadas, A. A. Demkov, Phys. Rev. B **90**, 125130 (2014)

[40] Y. Long, Y. Kaneko, S. Ishiwata, Y. Taguchi, Y. Tokura, J. Phys. Condens. Matter **23**, 245601 (2011)

[41] H. Monkhorst, J. Pack, Phys. Rev. B **13**, 5188 (1976)

[42] P. Blöchl, O. Jepsen, O. Andersen, Phys. Rev. B **49**, 16223 (1994)

[43] K. Fredrickson, P. Ponath, A. B. Posadas, M. McCartney, T. Aoki, D. J. Smith, A. A Demkov, Appl. Phys. Lett. **104**, 242908 (2014)

[44] P. Ponath, K. Fredrickson, A. B. Posadas, Y. Ren, X. Wu, R. K. Vasudevan, M. B. Okatan, S. Jesse, T. Aoki, M. R. McCartney, D. J. Smith, S. V. Kalinin, K. Lai, A. A. Demkov, Nat. Commun. **6**, 6067 (2015)

[45] J. F. Moulder, W. F. Stickle, P. E. Sobol, K. D. Bomben, Handbook of X-Ray Photoelectron Spectroscopy (Physical Electronics, Inc., Eden Prairie, 1995)

[46] L. Miranda, K. Boulahya, M. Hernando, D. C. Sinclair, F. Jimenez-Villacorta, A. Varela, J. M. Gonzalez-Calbet, M. Parras, Chem. Mater. **23**, 1050-1060 (2011)

[47] J. G. Dickson, L. Katz, R. Ward, J. Am. Chem. Soc. **83**, 3026-3029 (1961)

[48] G. M. Keith, M. J. Rampling, K. Sarma, N. Mc Alford, D. C. Sinclair, J. Eur. Ceram. Soc. **24**, 1721-1724 (2004)

[49] J. Wang, H. Zhang, D. Xue, Z. Li, J. Phys. D: Appl. Phys. **42**, 235103 (2009)

[50] C. Li, D. Cui, Y. Zhou, H. Lu, Z. Chen, Appl. Surf. Sci. **136**, 173 (1998)

[51] H. Nakayama, H. Katayama-Yoshida, Jpn. J. Appl. Phys. **40**, 1355 (2001)

[52] C. Mitra, AIP Adv. **2**, 032148 (2012)

[53] E. Blokhin, E. Kotomin, A. Kuzmin, J. Purans, R. Evarestov, J. Maier, Appl. Phys. Lett. **102**, 112913 (2013)

[54] K. H. Haerdtl, R Wernicke, Solid State Commun. **10**, 153-157 (1972)

[55] D. Cao, B. Liu, H. Yu, W. Hu, M. Cai, Eur. Phys. J. B **88**, 75 (2015)

[56] J. M. Florez, S. P. Ong, M. C. Onbasli, G. F. Dionne, P. Vargas, G. Ceder, C. A. Ross, Appl. Phys. Lett. **100**, 252904 (2012)

[57] K. G. Roberts, M. Varela, S. Rashkeev, S. T. Pantelides, S. J. Pennycook, K. M. Krishnan, Phys. Rev. B. **78**, 014409 (2008)

Figures

Figure 1: RHEED patterns of: a) 15%; b) 25%; c) 30%; and d) 40%; Co-substituted BTO films on STO(001) taken along the [100] direction. The BTCO thickness in all samples is 16 nm.

Figure 2: Typical x-ray diffraction 2θ-θ scan of 5% Co-substituted BTO film on STO/Ge. The film thickness is 10 nm. Only peaks from the substrate Ge as well as from STO and BTCO are observed.

Figure 3: a) High resolution cross-section TEM image for a 25% Co-substituted BTO film on 5 unit cells $SrTiO_3$ on Ge. High crystallinity and a sharp interface between the STO buffer and BTCO film is confirmed. b) EDXS line profile through the BTCO layer: a homogenous distribution of the Co atoms parallel to the interface is clearly shown, excluding the formation of Co clusters. c) & d) EELS measurements performed at 6 different positions in the sample. Ti atoms close to the Ge interface exhibit an oxidation state of +4 as can be seen by the splitting of the Ti L-edges. The gradual disappearance of the split closer to the surface indicates the presence of some Ti atoms with an oxidation state of +3, which is attributed to a sample preparation artifact due to argon-ion milling in thinner regions.

Figure 4: a) AFM Topography, b) Vertical BE-PFM Amplitude, and associated c) Vertical BE-PFM Phase after a box-in-box poling experiment. A box of size 5×5 μm^2 is poled with the tip held at -5V, and a smaller box of size 2×2 μm^2 within the larger square is poled with the tip held at +5V. On the same sample, 100 hysteresis loops are acquired with BE-spectroscopy across a 10×10 spatial grid, with the average of the 100 loops shown in d) Amplitude, and e) Phase plots.

Figure 5: a) Magnetization vs. field measurement at 5 K for a nominally 25% Co-substituted BTCO film on an STO single crystal (001) substrate. No hysteresis curve could be obtained, confirming the absence of ferromagnetism. b) Magnetization vs. temperature scan shows no temperature dependency for the measured film.

Figure 6: Atomistic arrangement, local site spin configuration, and projected density of states for a pair of cobalt atoms with no vacancies in a $3 \times 2 \times 2$ supercell showing that this configuration, found to be lowest in energy, is both metallic and has a net magnetic moment.

Figure 7: Atomistic arrangement, local site spin configuration, and projected density of states for a Co^{3+} configuration consisting of two cobalt atoms and a vacancy in a $3 \times 2 \times 2$ supercell. The lowest energy spin configuration results in two antiparallel high-spin atoms (no net moment) and an insulator.

Figure 8: Atomistic arrangement, local site spin configuration, and projected density of states for a Co^{2+} configuration (two cobalt atoms and two oxygen vacancies in a $3 \times 2 \times 2$ supercell which results in an insulating state with an antiparallel spin alignment (no net moment).

Figure 1:

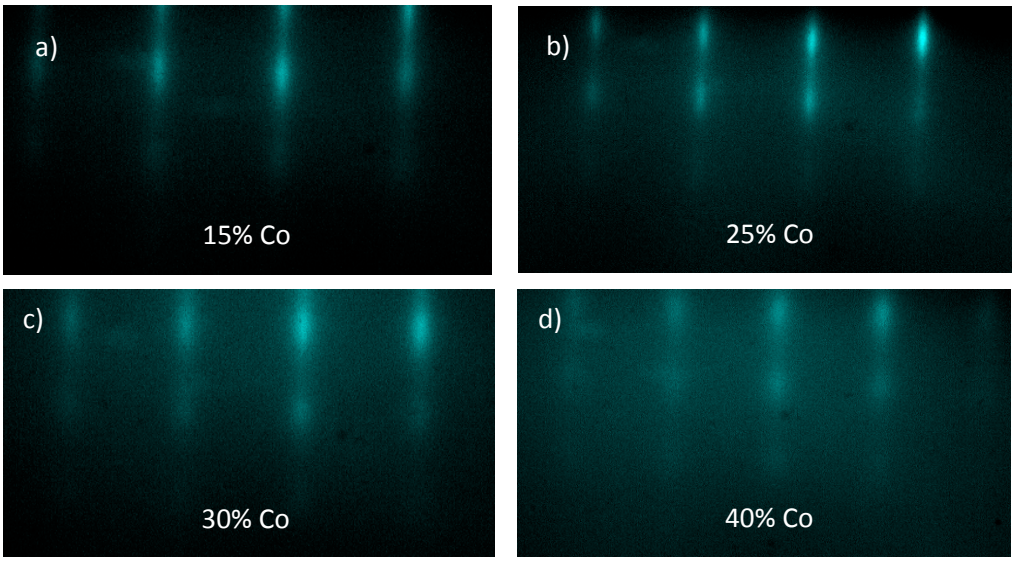

Figure 2:

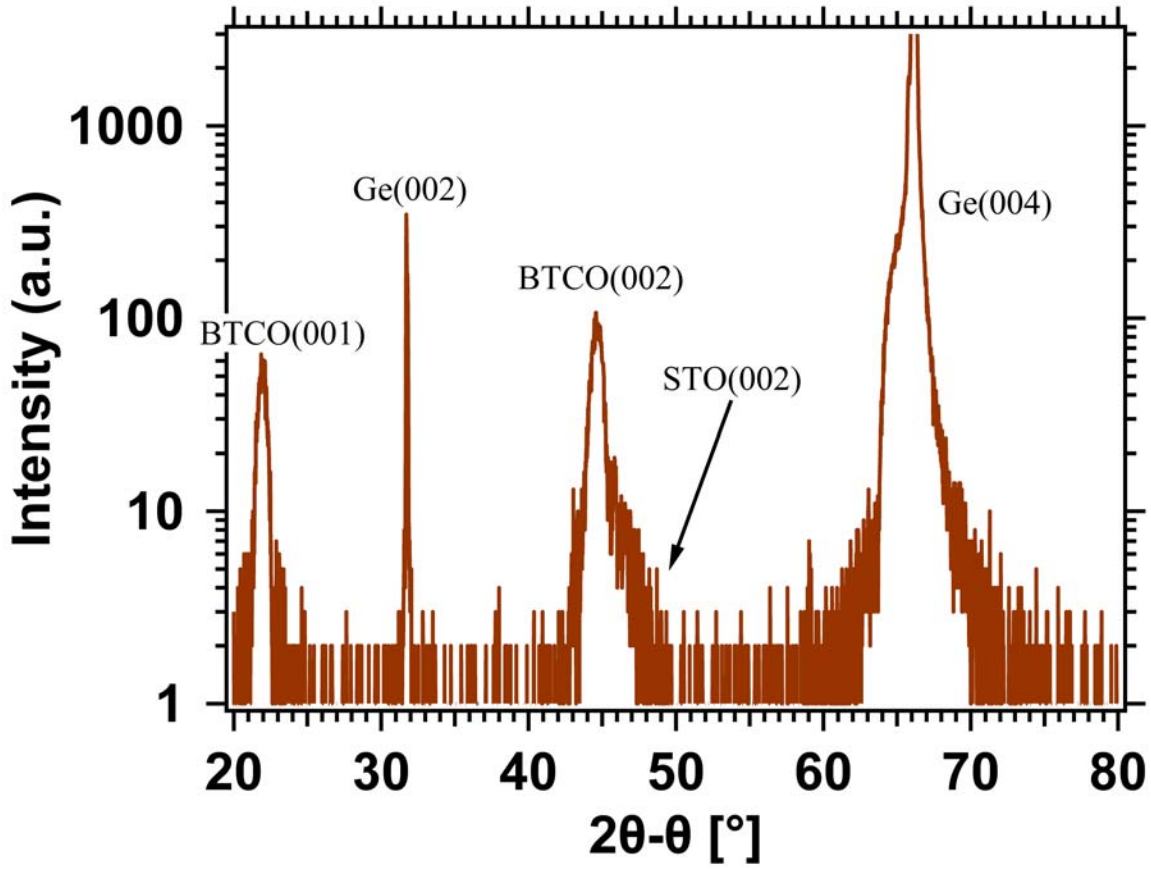
1000
100
10
1
Intensity (a.u.)
20
30
40
50
60
70
80
2θ-θ [°]
BTCO(001)
Ge(002)
BTCO(002)
STO(002)
Ge(004)

Figure 3:

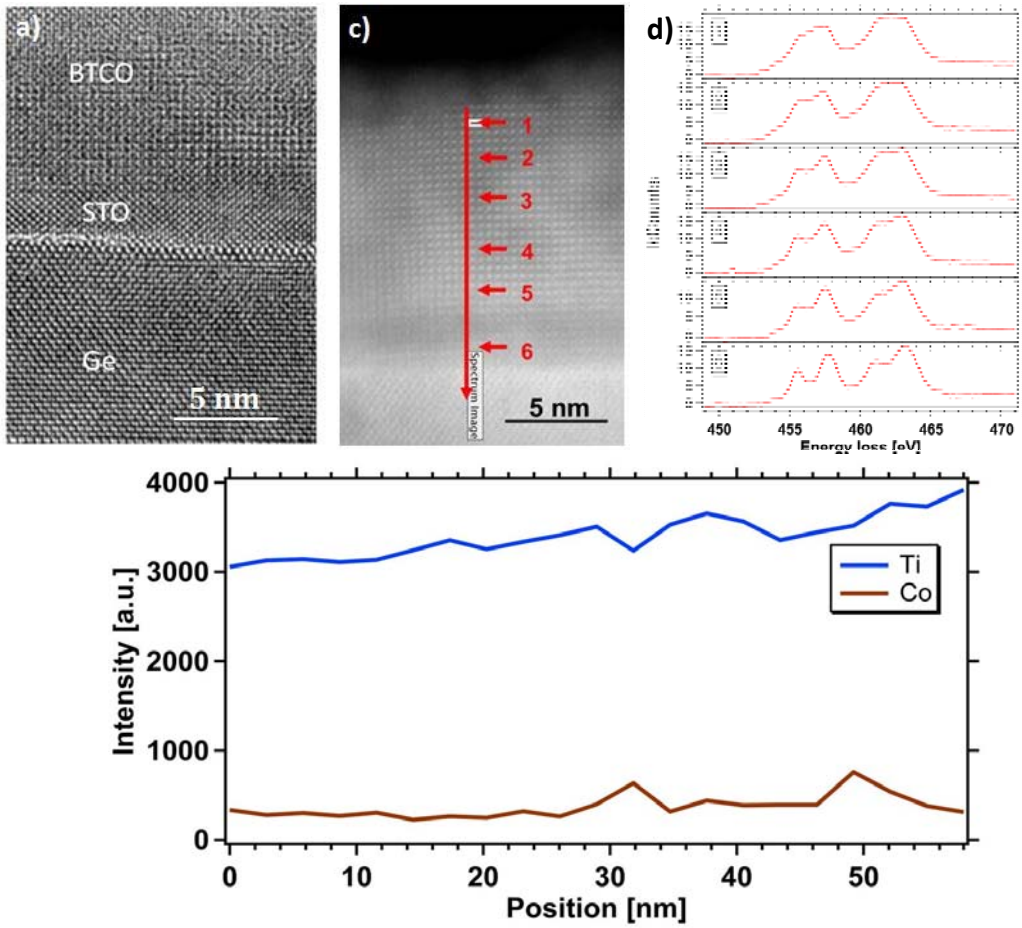
a)
BTCO
STO
Ge
5 nm
c)
1
2
3
4
5
6
5 nm
d)
450
455
460
465
470
Energy loss [eV]
4000
3000
2000
1000
0
Intensity [a.u.]
0
10
20
30
40
50
Position [nm]
Ti
Co

Figure 4:

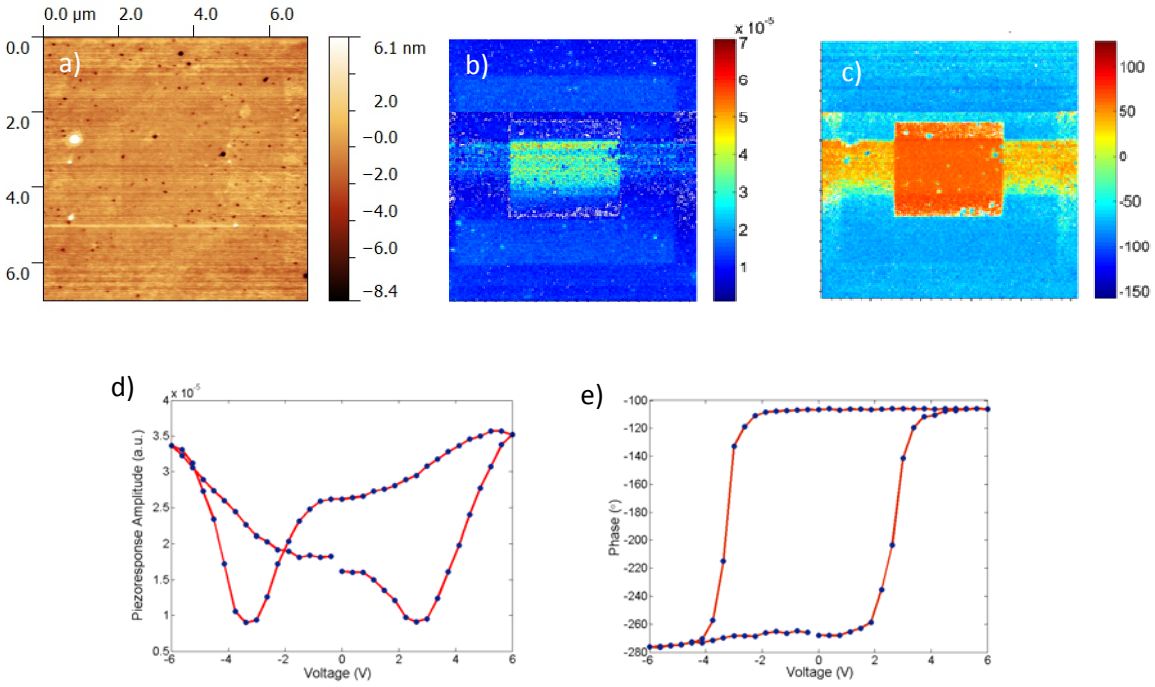
a)
0.0 µm
2.0
4.0
6.0
6.1 nm
2.0
−0.0
−2.0
−4.0
−6.0
−8.4
b)
x 10^-5
7
6
5
4
3
2
1
c)
100
50
0
-50
-100
-150
d)
x 10^-5
Piezoresponse Amplitude (a.u.)
Voltage (V)
e)
Phase (°)
Voltage (V)

Figure 5:

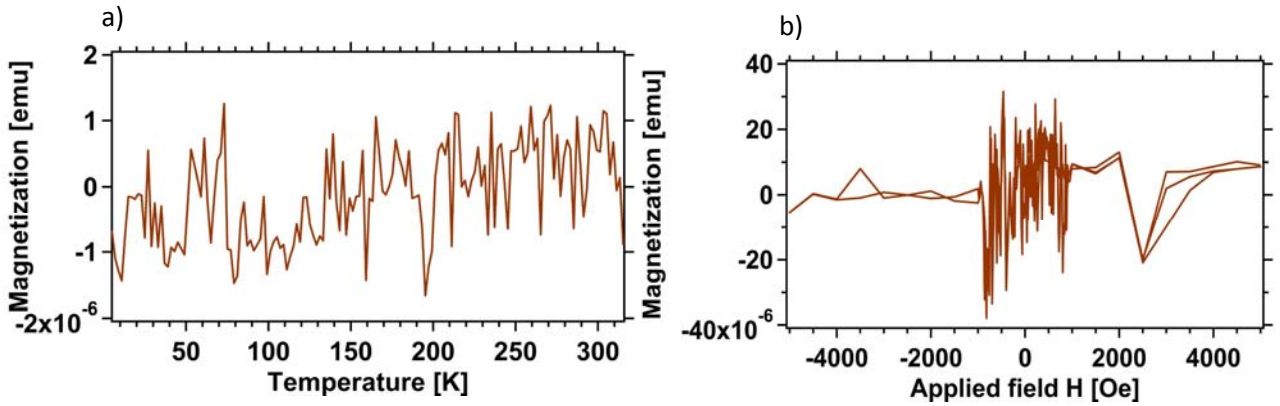
a)
Magnetization [emu]
2
1
0
-1
-2x10^-6
50
100
150
200
250
300
Temperature [K]
Magnetization [emu]
b)
40
20
0
-20
-40x10^-6
-4000
-2000
0
2000
4000
Applied field H [Oe]

Figure 6:

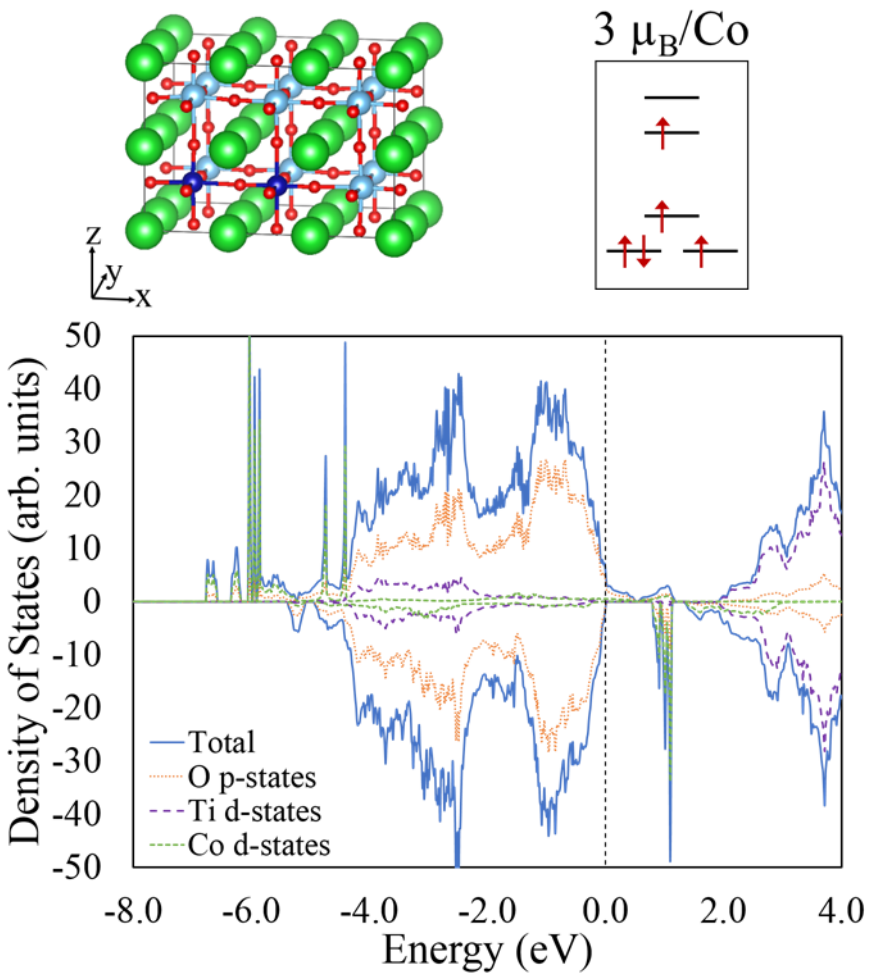
3 μB/Co
z
y
x
Density of States (arb. units)
50
40
30
20
10
0
-10
-20
-30
-40
-50
-8.0
-6.0
-4.0
-2.0
0.0
2.0
4.0
Energy (eV)
Total
O p-states
Ti d-states
Co d-states

Figure 7:

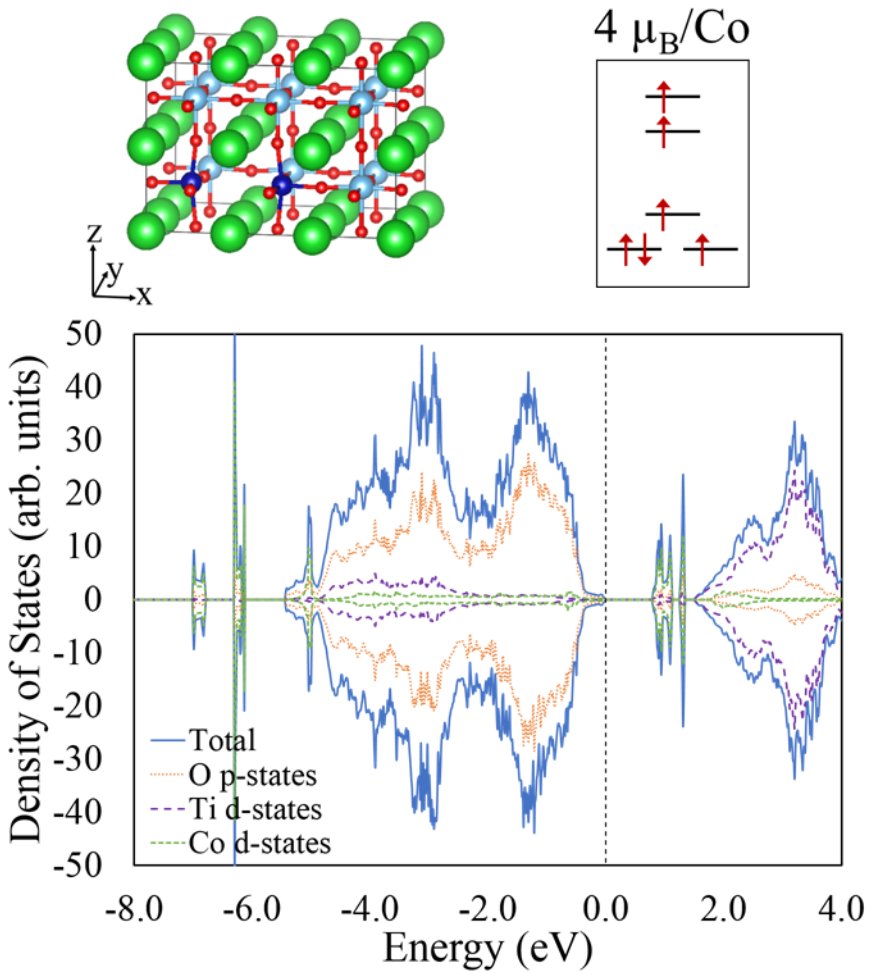
4 μB/Co
z
y
x
Density of States (arb. units)
50
40
30
20
10
0
-10
-20
-30
-40
-50
Total
O p-states
Ti d-states
Co d-states
-8.0
-6.0
-4.0
-2.0
0.0
2.0
4.0
Energy (eV)

Figure 8:

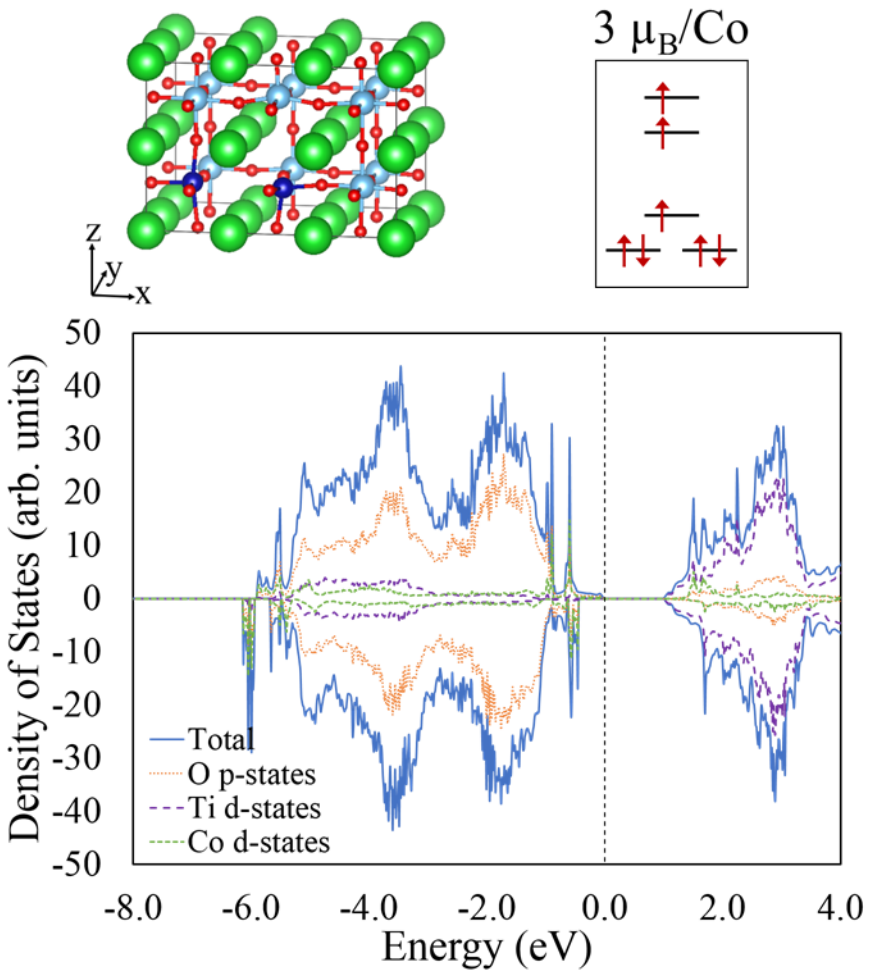
3 μB/Co
z
y
x
Density of States (arb. units)
50
40
30
20
10
0
-10
-20
-30
-40
-50
Total
O p-states
Ti d-states
Co d-states
-8.0
-6.0
-4.0
-2.0
0.0
2.0
4.0
Energy (eV)